Evaluation of a numerical simulation for multibipolar radiofrequency ablation

Christina A. Neizert, David Sinden, Christian Rieder, Tobias Preusser, Hanne Ballhausen, Ole Gemeinhardt, Kai S. Lehmann, Franz G. M. Poch

Angaben zur Veröffentlichung / Publication details:

Neizert, Christina A., David Sinden, Christian Rieder, Tobias Preusser, Hanne Ballhausen, Ole Gemeinhardt, Kai S. Lehmann, and Franz G. M. Poch. 2026. "Evaluation of a numerical simulation for multibipolar radiofrequency ablation." *International Journal of Hyperthermia* 43 (1): 2657470. https://doi.org/10.1080/02656736.2026.2657470.

International Journal of Hyperthermia

ISSN: 0265-6736 (Print) 1464-5157 (Online) Journal homepage: www.tandfonline.com/journals/ihyt20

Evaluation of a numerical simulation for multibipolar radiofrequency ablation

Christina A. Neizert, David Sinden, Christian Rieder , Tobias Preusser , Hanne Ballhausen , Ole Gemeinhardt , Kai S. Lehmann & Franz G. M. Poch

To cite this article: Christina A. Neizert, David Sinden, Christian Rieder , Tobias Preusser , Hanne Ballhausen , Ole Gemeinhardt , Kai S. Lehmann & Franz G. M. Poch (2026) Evaluation of a numerical simulation for multibipolar radiofrequency ablation, International Journal of Hyperthermia, 43:1, 2657470, DOI: 10.1080/02656736.2026.2657470

To link to this article: https://doi.org/10.1080/02656736.2026.2657470

INTERNATIONAL JOURNAL OF HYPERTHERMIA
2026, VOL. 43, NO. 1, 2657470
https://doi.org/10.1080/02656736.2026.2657470

Evaluation of a numerical simulation for multibipolar radiofrequency ablation

Christina A. Neizert[a], David Sinden[b], Christian Rieder[c], Tobias Preusser[c], Hanne Ballhausen[d], Ole Gemeinhardt[e], Kai S. Lehmann[e] and Franz G. M. Poch[a]

[a]Department of General, Visceral, Transplantation and Thoracic Surgery, Universitätsklinikum Augsburg, Augsburg, Germany; [b]Department of Image Guided Therapy, Fraunhofer Institute for Digital Medicine MEVIS, Bremen, Germany; [c]TechsoMed GmbH, Bremen, Germany; [d]Department of Mathematics, Universität Bremen, Bremen, Germany; [e]Department of General and Visceral Surgery, Charité – Universitätsmedizin Berlin, Freie Universität Berlin and Humboldt-Universität zu Berlin, Berlin, Germany

ABSTRACT

Introduction: The aim of this study was to assess the accuracy of a custom-developed numerical simulation of hepatic multibipolar radiofrequency ablation (mbRFA) under standardized conditions, accounting for temperature-dependent changes in tissue properties, dehydration and coagulation. The model was specifically assessed for its ability to predict vascular cooling effects induced by large vessels using an established *ex vivo* porcine liver model. A GPU-accelerated finite-difference time-domain (FDTD) simulation coupling the quasi-static Maxwell and Pennes' bioheat equations was implemented to model mbRFA.

Methods: *Ex vivo* mbRFA were performed using three internally cooled bipolar applicators. A saline-perfused glass tube was employed to simulate a standardized blood flow and positioned at five predefined distances from the ablation center in 2.5 mm increments. Simulated and experimental ablations were compared using area-, surface- and classification-based metrics on a standardized two-dimensional (2D) cross section to evaluate the model's predictive accuracy.

Results: The numerical simulation reliably predicted the ablation shape for mbRFA while effectively accounting for vascular cooling effects. Conformity between simulated and real ablation areas was 96% across all experimental settings. The average similarity between the *ex vivo* ablations and the simulation were 0.92 (Dice coefficient) and 0.85 (Jaccard coefficient), respectively. Compared to the reference area, the simulation overestimated the ablation zone by 4% (false-positive regions) and underestimated it by 10% (false-negative regions).

Conclusion: Overall, the numerical model demonstrated good spatial agreement with the experimental ablations, confirming its suitability for quantitative prediction of ablation geometry.

ARTICLE HISTORY
Received 26 October 2025
Revised 25 March 2026
Accepted 4 April 2026

KEYWORDS
Radiofrequency ablation; multibipolar; numerical simulation; cooling effects; liver

Introduction

Radiofrequency ablation (RFA) is a well-established minimally invasive treatment option for patients with primary and secondary malignant liver tumors [1,2]. RFA is particularly beneficial for small tumors, individuals with unfavorable tumor locations, impaired liver function or significant comorbidities [2–4]. Alongside microwave ablation (MWA), RFA is currently one of the most frequently used procedures for liver tumor ablation [5]. Conventional RFA, typically performed in mono- or bipolar mode, delivers high-frequency alternating current into the liver tissue via a single applicator, effectively treating tumors up to 3 cm in size [1,4]. However, local recurrence rates ranging up to 40% have been reported for RFA, highlighting its limitations, particularly for larger tumors or those located near major hepatic vessels [3,6–8]. These challenges are largely attributed to the 'heat sink effect', where the natural liver perfusion advects thermal energy from the ablation site reducing the efficacy of RFA [9].

To address these limitations, advancements in RFA technology have led to the development of multibipolar RFA (mbRFA) [7,10]. In mbRFA multiple bipolar electrodes are strategically placed around the tumor in a 'no-touch' configuration, allowing high-density electrical currents to flow exclusively between

CONTACT Christina A. Neizert christina.neizert@uk-augsburg.de Department of General, Visceral, Transplantation and Thoracic Surgery, University Hospital of Augsburg, Stenglinstraße 2, 86156 Augsburg, Germany.

the electrodes [11]. By avoiding direct tumor contact, the risk of needle track seeding is minimized. Additionally, mbRFA generates larger and more uniform ablation zones, enabling effective treatment of tumors larger than 3 cm while also ensuring an adequate peritumoral safety margin [12].

Technical success of in-situ procedures can only be assessed indirectly through imaging techniques like magnetic resonance imaging (MRI) or contrast-enhanced computed tomography (CECT) or ultrasound (CEUS) [2,13,14]. Accurate pre-interventional planning is essential to achieve sufficient ablation margins and minimize the risk of local recurrence in mbRFA. Treatment planning algorithms assist in predicting ablation size and shape, optimizing parameters and guiding applicator positioning. Various computational models and validation methods have been developed to support these efforts [15–20]. However, simulation accuracy is influenced by patient- and device-specific factors, such as liver tissue characteristics (cirrhosis, tumor, chemotherapy-treated, etc.), tumor size, thermal conductivity, tissue impedance, the ablation device and the set ablation parameters [19]. Among these, vascular cooling effects and the patient's unique intrahepatic vascular anatomy remain particularly challenging to model accurately. While incorporating all relevant parameters could theoretically enhance accuracy, this comes with an increased complexity and computational burden. Additionally, most simulation models are designed for monopolar and bipolar RFA configurations, leaving advanced techniques like mbRFA unaddressed [15,18,21–23]. Placement of multiple electrodes in close proximity leads to overlapping thermal fields that act synergistically, producing higher local temperatures and disproportionately larger ablation zones. Such interactions, considerably complicate the prediction of the overall ablation volume [23].

Rieder et al. developed a simulation software for mbRFA that approximates the ablation zone while also accounting for vascular cooling effects of hepatic vessels [24]. However, this software has not been validated experimentally yet. Experimental validation, particularly through *ex vivo* studies, is critical to ensure a software's accuracy and reliability for clinical use [25]. These validations also help to confirm the software's ability to predict key factors, such as ablation size and shape, while addressing biological complexities like tissue variability and the heat-sink effect.

The objective of this study was a systematic evaluation of the numerical simulation software for *ex vivo* mbRFA, with a particular focus on its incorporation of vascular cooling effects.

Material and methods

Multibipolar radiofrequency ablation

Multibipolar radiofrequency ablations (mbRFA) were performed in an established *ex vivo* model with native porcine livers, that were obtained from an abattoir [26–29]. All experiments were carried out at room temperature within six hours after slaughtering. A multibipolar ablation system (CelonPOWER System, Olympus Surgical Technologies Europe, Hamburg, Germany), consisting of a power control unit (CelonLab POWER, Olympus Surgical Technologies Europe, Hamburg, Germany) and a triple peristaltic pump (CelonAquaflowIII, Olympus Surgical Technologies Europe, Hamburg, Germany) for internal applicator cooling was used. Energy delivery was controlled by a resistance controlled automatic power mode (RCAP) through three internally cooled bipolar applicators (CelonProSurge T-20, Olympus Surgical Technologies Europe, Hamburg, Germany) with an active tip length of 20 mm and a diameter of 1.8 mm. The three applicators were arranged in parallel in a triangular configuration within the porcine liver, with a fixed spacing of 20 mm between them. Precise placement was ensured using a custom-made aiming device (Figure 1(a)).

A total power of 60 W was preset on the generator according to the manufacturer's recommendations. Ablations were manually terminated after reaching an energy input of 40 kJ. Previous studies have systematically evaluated vessel diameters and flow rates within clinically relevant ranges, demonstrating that neither parameter substantially influences the extent of vascular cooling or ablation zone deformation in thermal ablations [29–34]. Accordingly, a single representative vessel configuration was employed to isolate positional effects. A glass tube ('vessel') with an inner diameter of 3.4 mm and an outer diameter of 5.0 mm served as an artificial vessel. A peristaltic pump (Watson Marlow Pumps 323E, Watson-Marlow Limited, Falmouth, Cornwall, UK) delivered room-temperature saline at a continuous flow rate of 100 ml/min. This flow rate was selected based on prior findings that cooling effects occur above

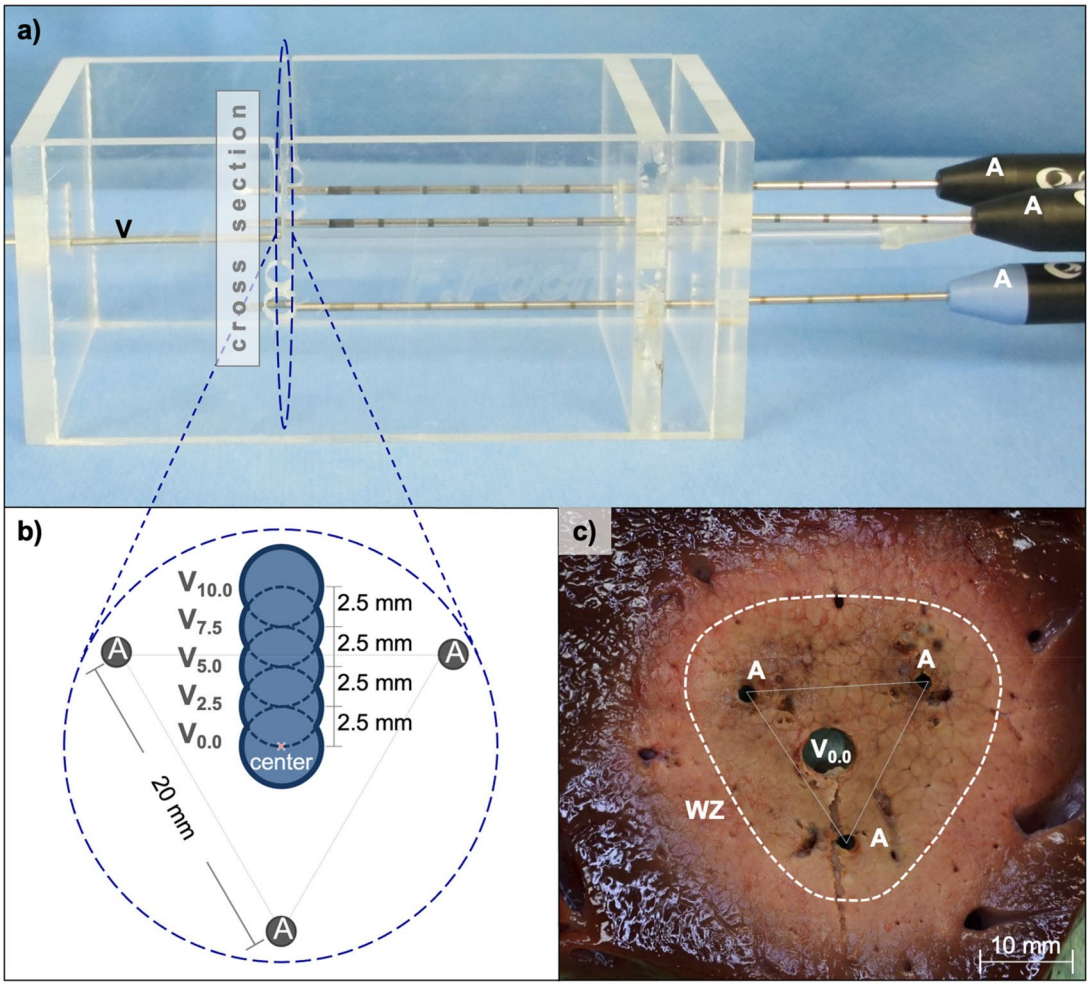

Figure 1. **a)** The custom-made aiming device ensured exact positioning of the three applicators (A) and the glass tube (V) into the liver tissue. It included a preset slit, allowing the liver to be precisely cut orthogonally to the applicators for a cross-sectional analysis. The liver was sectioned into smaller pieces of approximately 5 × 5 × 7 cm to fit into the aiming device. **b)** Illustration of the experimental setup in the cutting plane: applicator spacing was set to 20 mm. Five different vessel-to-center distances were assessed ($V_{0.0}$, $V_{2.5}$, $V_{5.0}$, $V_{7.5}$ and $V_{10.0}$). **c)** Exemplary *ex vivo* cross section of a test series with a centrally placed vessel ($V_{0.0}$).

10 ml/min and plateau at higher rates [29,31–34]. The study design therefore focused on the spatial relationship between the vessel and the applicators, with the vessel positioned parallel to the applicators (Figure 1(a)). Five different experimental settings (each $n = 6$) were planned (Figure 1(b)):

- $\mathbf{V}_{0.0}$ = vessel situated in the ablation center (geometrical center point of the three applicators)
- $\mathbf{V}_{2.5}$ = vessel situated 2.5 mm away from the center (on a bisector of the three applicators)
- $\mathbf{V}_{5.0}$ = vessel situated 5.0 mm away from the center
- $\mathbf{V}_{7.5}$ = vessel situated 7.5 mm away from the center
- $\mathbf{V}_{10.0}$ = vessel situated 10.0 mm away from the center

After mbRFA, ablations were bisected orthogonally to the applicators at the level of the insulator – positioned between the two electrodes of each applicator – to achieve the largest cross-sectional area and ensure a consistent and reproducible cutting process (Figure 1(c)). This procedure was applied identically to all ablations. The ablation halves were photographed next to a millimeter scale. Subsequently, the photographs were imported into a custom-made analysis software previously developed by the Fraunhofer Institute for Digital Medicine MEVIS (Bremen, Germany) for RFA [17,24]. The software performs an initial calibration of the photograph, computationally corrects distortions caused by cutting the liver specimen using a thin-plate spline landmark registration and outlines the ablation area [24]. Ablation

geometry and size of the so-called white zone (WZ) were measured, with the WZ referring to an ablation area where the liver tissue has undergone irreversible damage [13,35,36] (Figure 1(c)). All photographs were geometrically aligned according to the position of the vessel and the three applicators for statistical analysis. Shape-based averaging was used to generate averaged 'necrosis masks' of the ablation area [37].

Numerical simulation

The computation of RFA proceeds iteratively: firstly, the heat source term is simulated using a quasi-static approximation to Maxwell's equations, then the thermal field is computed. The thermal field subsequently drives dose field calculation. Next, material properties are updated from the thermal field and the source term is recomputed [19]. Then both the thermal and dose fields are recalculated using the updated material properties for the new time value. The mathematical model used for the simulation of mbRFA was derived from an existing numerical simulation for mono- and bipolar RFA, which solves the quasi-static Maxwell equation [22]

$$\nabla\left(\sigma\cdot\nabla\varphi\right)=0 \tag{1}$$

where φ is the electric potential, so that $\nabla\varphi$ represents the electric field and σ [A/(V·m)] is the spatially and thermally dependent electrical conductivity (Appendix A). The source term, q, is computed using the position in the tissue and knowledge of the specific applicator geometry. Nonzero Dirichlet boundary conditions are imposed at the electrode surfaces, where the electric potential φ is fixed according to the applied bipolar voltage. The exterior boundary conditions assume the computational domain is sufficiently large so that φ = 0.

The absorbed energy is modeled via Joule heating and is proportional to the square of the voltage, that is,

$$q=\lambda\sigma\left|\nabla\varphi\right|^2\left[W/m^3\right], \tag{2}$$

where the scaling factor λ accounts for the efficiency of the device, given by the ratio of the effective power, p_{eff} and the total power, p_{total}.

$$p_{\text{eff}}=\frac{4\,p_{\text{setup}}R_{\text{tissue}}R_{\text{I}}}{\left(R_{\text{tissue}}+R_{\text{I}}\right)^2} \tag{3}$$

$$R_{\text{tissue}}=\frac{U^2}{p_{\text{total}}} \tag{4}$$

$$p_{total}=\int\sigma\left|\nabla\varphi\right|^2dx, \tag{5}$$

where p_{setup} is the driving power, R_I is the internal resistance of the generator [Ω], R_{tissue} denotes the electrical resistance of the tissue and U[V] is the difference between the potential on each electrode, i.e. U= 2V as bipolar.

As the electrodes were internally cooled, a Dirichlet boundary condition was imposed for the electrodes, fixing the temperature as the ambient temperature. To model the heat sink effect of large vessels, an interior Dirichlet condition was also imposed, and the temperature within the vessel fixed to the temperature of the saline solution, which is used in Penne's bioheat transfer equation, which computes the temperature T via

$$\rho c_v\frac{\partial T}{\partial t}=\nabla\cdot\left(k\cdot\nabla T\right)+q \tag{6}$$

In this equation ρ is the density [kg/m^3], c_v is the specific heat capacity [J/(K·kg)] and k the thermal conductivity [W/(K·m)] (Appendix A).

The multibipolar model used in this study is based on a previously developed and experimentally validated numerical framework for mono- and bipolar hepatic RFA by Kroeger and Rieder et al. [17,21,22,24,38]. In the present work, this framework was extended to a multibipolar applicator

configuration and adapted to the experimental setup with a saline-perfused, vessel-mimicking glass tube. The model employs a coupled system of two partial differential equations to simulate temperature progression over time [22,24,38]. The modeling of electrical conductivity was based on former experiments with porcine liver and incorporated the combined effects of temperature, dehydration and coagulation factors derived from an Arrhenius damage model [22,39]. Phase transitions and evaporation were simulated using a predictor-corrector scheme to account for tissue dehydration, which significantly affects heat transfer and electrical conductivity.

In our *ex vivo* experiments, vessel cooling was induced by a saline-perfused glass tube, numerically modeled as a Dirichlet boundary condition at constant saline temperature to reproduce experimental conditions rather than capture the full complexity of *in vivo* hepatic perfusion. The heat sink effect was modeled with Pennes' bioheat equation, while the Arrhenius equation was used to determine tissue damage [40]:

$$\Omega = \int A_0 e^{-E_a/(R_g T(t))} dt \tag{7}$$

where the R_g= 8.314 [J mol/K] is the universal gas constant and the Arrhenius parameters for liver tissue are given by A_0= 7.39×10^{39} [1/s] and E_a= 257,700 [J/mol] (Appendix A). The governing equations were solved using finite-difference time-domain methods which were first order accurate in time, and second order accurate in space. The discretized system was solved using a GPU using a preconditioned conjugate-gradient solver exploiting the sparsity of the system. The spatial resolution was set to 1 mm, which could resolve the glass vessel. The domain sizes were (128, 128, 128). The Courant-Fredrichs-Lewy number did not exceed 0.3. Ablation volumes were computed by summing the voxels with ' ≥1.Convergence tests were performed on the spatial resolution to ensure that ablation volumes were the same as finer resolution simulations.

Data analysis

Macroscopical ablation zones (G=*ground truth)* were statistically compared to the numerically simulated ablation zones (S=*simulation)* in order to validate the accuracy of the software. The two necrosis masks were compared quantitatively using the following area, surface and classification-based measures:

The Dice and Jaccard coefficients were calculated for an area-based comparison. The Dice coefficient quantifies the similarity of two sets G and S, with values ranging from 0 to 1 [41]. It is calculated by dividing twice the intersection of the two sets by the sum of their areas, expressed as $\frac{2|G\cap S|}{|G|+|S|}$. The Jaccard coefficient measures the proportion of the intersection area relative to the union of both sets, also ranging from 0 to 1 [42]. It is defined as $\frac{|G\cap S|}{|G\cup S|}$, where $|G\cap S|$ represents the size of their intersection and $|G\cup S|$ denotes the size of their union. For a surface-based comparison, the Hausdorff distance was employed, quantifying the maximum of the shortest distances between points on the simulation mask and their nearest counterparts on the *ex vivo* necrosis mask. The maximum surface distance ($\max_{s\in S} d(s,G)$) and the mean surface distance ($mean_{s\in S}\, d(s,G)$) were determined. Additionally, the false positive rate (FP) and the false negative rate (FN) were calculated to assess simulation accuracy. The FP rate, $FP=|S|-|G|$, reflects the extent of overestimation of the simulation, while the FN rate, $FN=|G|-|S|$, indicates underestimation (Figure 2). The true positive rate, $TP=|G\cap S|$, represents the intersection of the simulation and the averaged necrosis mask of each experimental setting, quantifying the area accurately predicted by the software. To validate the simulation against *ex vivo* results, classification-based metrics were applied to evaluate the agreement between the masks. Typically, sensitivity $\frac{TP}{TP+FN}$ and specificity $\frac{TN}{TN+FP}$ are employed. However, specificity depends on the true negative (TN) rate, which corresponds to the image background. As a result, it is influenced by the size of the selected image rather than the extracted mask. Therefore, the positive predictive value $\left(PPV=\frac{TP}{TP+FP}\right)$ was applied instead.

SPSS (IBM SPSS Statistics, version 29 for Windows, Armonk, USA) was used for statistical analysis. To characterize the distribution and stability of summary statistics in the presence of small sample sizes

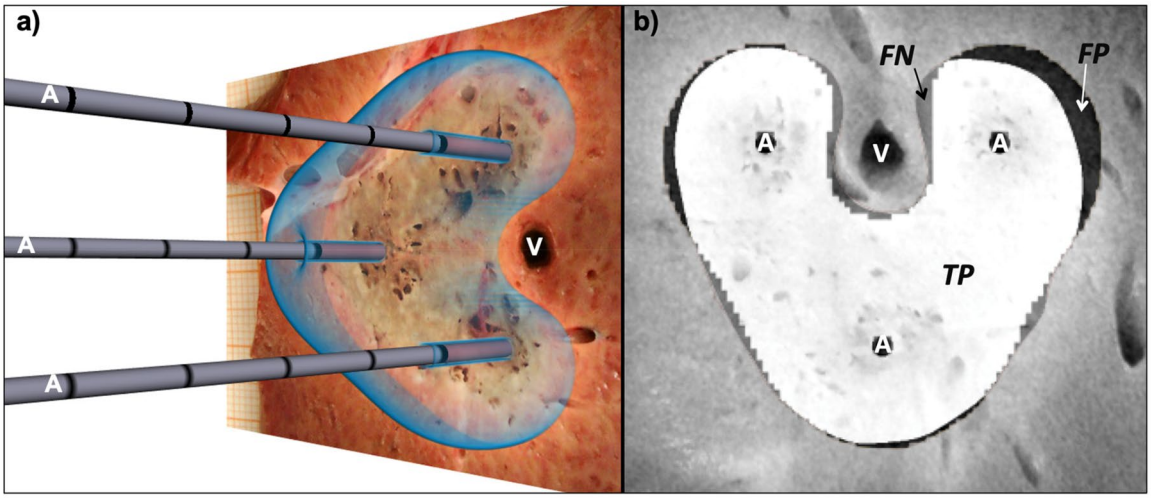

Figure 2. **a)** Example of the simulation software and **b)** a shape-based averaged necrosis mask with overlays of FP (dark grey), FN (medium grey) and TP (light grey) masks. A: applicator; V: vessel; TP: true positive; FP: false positive; FN: false negative.

($n = 6$ per distance), the robustness of mean-based measures was evaluated using coefficient of variation, interquartile range (IQR)-based outlier detection and non-parametric bootstrapping (10,000 resamples) to obtain 95% confidence intervals. For descriptive reporting, mean ± standard deviation (SD) was used as the primary summary measure; median and IQR were additionally calculated to assess sensitivity to data dispersion. Ablation times were compared between groups defined by vessel distance using the non-parametric Kruskal-Wallis test.

Data availability statement

The datasets analyzed in our study are available from the corresponding author on reasonable request.

Results

In total, 30 mbRFA with five different ablation settings ($n = 6$) were conducted. The cross-sectional ablation area was 914 mm^2 (715–1318 mm^2). The mean ablation time was 25 min and 39 s (mean ± SD: 1539 ± 98 s). No difference in ablation time was observed between the different experimental groups ($p \geq 0.05$).

The average similarity between necrosis mask and simulation was 0.92 (Dice coefficient) and 0.85 (Jaccard coefficient; Figure 3(a)), respectively. The average area of congruency (TP) between the necrosis mask and the simulation was 816 mm^2, resulting in a PPV of 96%. The numerical simulation underestimated (FN) the thermal necrosis by 10% (94 mm^2; Figure 3(b)). Therefore, the sensitivity of the simulation was 90%. The surface distance between the simulation and the regions where the software underestimated necrosis (FN), was 0.9 mm (median) and 2.8 mm (maximum), respectively (Figure 3(c)). Overestimation of necrosis (FP), which potentially is relevant for local tumor recurrence after RFA, was 4% (35 mm^2; Figure 3(b)). The surface distances for FP were 0.5 mm (median) and 1.5 mm (maximum), respectively. The mean surface distance remained within the simulation's sampling accuracy, as the voxel size of the computational domain was 0.5 mm (Figure 3(c)).

The accuracy of the simulated calculations was influenced by the vessel's position. False negative results (FN, underestimation) increased as the vessel positioned was further away from the ablation center. False positive results (FP, overestimation) exhibited an inverse relationship, decreasing with greater vessel distance (Figure 4, Table 1).

Table 1 shows the corresponding areas between ablation masks and numerical simulation. For Area TP, the low coefficients of variation together with the narrow bootstrap confidence intervals indicated that the mean was a stable estimate. Mean ± SD was therefore considered representative for this

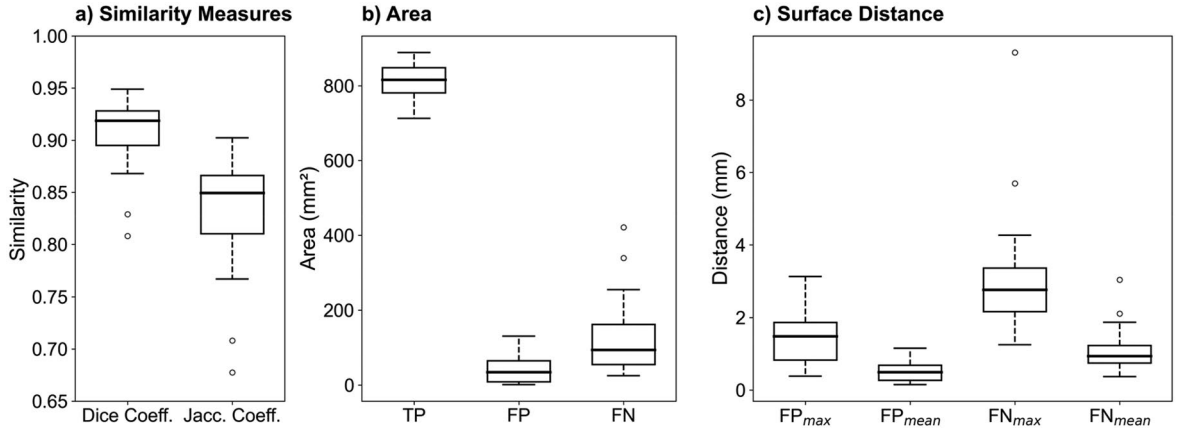

Figure 3. **a)** Average Dice and Jaccard coefficients marking average similarity between the simulation and the *ex vivo* necrosis marks. **b)** Values for the overestimated area (FP), the underestimated area (FN) and the area of congruency between the simulation and the measured necrosis mask (TP). **c)** Maximum as well as mean distances from measured necrosis surface distance to the underestimated (FN) and overestimated surface (FP) distance are shown.

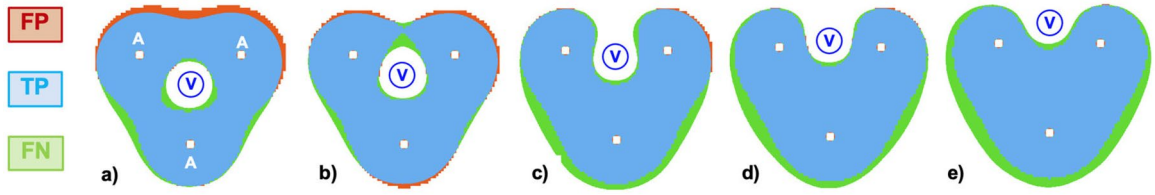

Figure 4. Shape-based averaged necrosis masks were generated with corresponding vessel distances from the center point: **a)** 0.0 mm, b) 2.5 mm, c) 5.0 mm, **d)** 7.5 mm and **e)** 10.0 mm with perfusion. Vascular cooling effects around the vessel (V) were observed in all test series. The blue mask indicates congruence (TP) between the measured *ex vivo* ablations and the simulation, orange represents overestimation (FP) and green denotes underestimation (FN) by the simulation. The voxel size of the numerical simulation was 0.5 mm.

Table 1. Median values for true positive (TP), false positive (FP) and false negative (FN) areas for all test series.

		Vessel distance from the ablation center				
		0 mm ($n=6$)	2.5 mm ($n=6$)	5.0 mm ($n=6$)	7.5 mm ($n=6$)	10.0 mm ($n=6$)
TP	Congruency (%)	92	92	98	98	99
	Area (mean ± SD, mm²)	784 ± 34	777 ± 45	799 ± 29	827 ± 26	877 ± 15
FP	Overestimation (%)	8	8	2	2	1
	Area (mean ± SD, mm²; *median [IQR]*)	75 ± 34 *69 [39]*	67 ± 44 *67 [60]*	30 ± 29 *18 [42]*	26 ± 26 *20 [45]*	13 ± 15 *9 [14]*
FN	Underestimation (%)	7	5	14	15	15
	Area (mean ± SD, mm²; *median [IQR]*)	67 ± 29 *63 [30]*	72 ± 63 *44 [61]*	142 ± 108 *129 [80]*	152 ± 96 *150 [166]*	188 ± 126 *155 [56]*

Data are presented as mean ± standard deviation (SD); n = number of samples per distance. For variables with higher variability (area FP and FN), median and interquartile range (IQR) are additionally reported to indicate robustness.

parameter. In contrast, Area FP and FN showed higher variability, evidenced by larger differences between mean and median as well as wider confidence bounds. To reflect this variability, median and IQR were additionally reported for these measures in Table 1. The underestimation (FN) of necrosis increased with increasing distance of the vessel from the center point, while the overestimation (FP) showed a negative relationship.

Discussion

This study aimed to validate a numerical planning software for multibipolar radiofrequency ablation (mbRFA) under *ex vivo* conditions. Five experimental setups were conducted using a perfused glass tube to mimic a hepatic vessel. The resulting macroscopic necrosis masks were compared with the corresponding simulation outputs to assess accuracy. Our results showed an overall conformity between the

simulated and actual ablation areas of 96% across all experimental settings. Similarity between the *ex vivo* ablations and the simulation were quantified by a Dice coefficient of 0.92 and a Jaccard coefficient of 0.85. Compared with the necrosis mask, the simulated ablation areas were overestimated by 4% (false-positive regions) and underestimated by 10% (false-negative regions).

Pre-therapeutic treatment planning is crucial in RFA, particularly because imaging modalities used to evaluate technical success have inherent limitations in their accuracy [13]. Ablation procedures are commonly planned according to manufacturer guidelines, which are normally derived from ablations performed under ideal conditions (*ex vivo* with the absence of vascular cooling effects). Software-based numerical simulations offer a more precise alternative by integrating patient-specific variables, including vascular cooling effects, liver tissue characteristics (cirrhosis, tumor, neoadjuvant therapy, etc.) and specific parameters of the ablation system [18,19,24,43]. The wide range of approaches, varying levels of accuracy and high computational demands make it challenging to identify a model suitable for clinical implementation [19]. Moreover, simulations for advanced techniques such as mbRFA are scarce [24].

Our findings demonstrate that the numerical simulation accurately predicted the ablation shape for mbRFA while incorporating vascular cooling effects. Congruency (TP) between the necrosis mask and the simulation was 96%. According to literature, Dice similarity coefficients describing the overlap between real and simulated RFA range from 0.42 to 0.73, with maximum surface deviations reported between 1.1 and 8.67 mm [19]. In comparison, our study demonstrated a much higher Dice coefficient of 0.92 and a maximum surface distance of 1.5 mm (FP regions) and 2.8 mm, respectively (FN regions; Figure 3(c)). However, it must be noted that replicating and predicting ablation zones *in vivo* is significantly more challenging due to factors such as tissue heterogeneity and blood perfusion. These complexities result in comparatively lower Dice coefficients and PPV values than those observed in controlled *ex vivo* experiments [19,22,44].

The numerical simulation examined in this study underestimated thermal necrosis (FN) by 10%, with a maximum false negative distance of 2.8 mm (Figure 3(c)). This indicates a potential risk of unintended tissue damage within 2.8 mm of the simulated necrosis. While it is essential to address these discrepancies to avoid unnecessary damage to adjacent healthy tissue, a small degree of underestimation may provide a safety margin during clinical application. To ensure complete and safe destruction of the target tissue, a safety margin of at least 5.0–10.0 mm around the ablation zone should be added [2,8,45]. This safety margin is consistent with guidelines for RFA procedures, which emphasize the importance of accounting for both thermal gradients and vascular cooling effects to reduce the risk of incomplete ablation or unintended tissue damage [3,45]. No universally accepted thresholds for metrics such as false positives/negatives, Hausdorff distance, Dice or Jaccard indices in the context of ablation simulation accuracy exist. This is why ablation margins are used in clinical practice: accuracy is assessed against a safety boundary that compensates for uncertainties in tumor shape, size and imaging. Thus, accuracy cannot be defined by absolute metric values alone but must always be interpreted in the context of the intended safety margin.

False positive (FP) regions, where the simulation predicts thermal destruction, but viable tumor tissue remains, are clinically significant due to their potential to cause local recurrence [46]. The most accurate simulation results were observed when the vessel was located at the ablation margin, with FP areas limited to just 1% for a vessel distance of 10 mm from the ablation center (Table 1). Conversely, when the vessel was positioned at the ablation center, the simulation overestimated the ablation by 8%. Errors in predicting ablation size can result in over- or under-treatment, posing specific risks to the patient [43]. Both false positive (FP) and false negative (FN) areas represent distinct clinical challenges in thermal ablation procedures. While FP regions can lead to local tumor recurrence due to incomplete ablation, FN regions increase the risk of unintentional thermal damage to adjacent organs or critical structures [47].

Overall, the numerical simulation demonstrated a strong correlation between the predicted necrosis masks and the actual thermal ablations observed, effectively modeling vascular cooling effects in mbRFA under standardized *ex vivo* conditions. The simulations could be extended by including effects of laminar flow of blood, however *in vivo* simulations may require detailed vascular maps, beyond the spatial resolution of many clinical imaging systems. Deformation due to thermal expansion, or coagulation could be incorporated to increase accuracy. Further *in vivo* studies are needed to validate these findings and refine the integration of numerical simulations into clinical practice.

Certain limitations of our study should be considered when interpreting the results. We used an established *ex vivo* porcine liver model in our study, as porcine liver is widely recognized for its anatomical and physiological resemblance to human liver tissue [26–29]. We consider *ex vivo* validation a necessary intermediate step before advancing to *in vivo* studies. Notably, ablation procedures are typically planned according to manufacturer guidelines, which are often based on data obtained under idealized *ex vivo* conditions [20,48]. To minimize inaccuracies due to autolysis, liver specimens were processed within six hours postmortem. While hepatocellular carcinoma (HCC) tumor models are available, we opted for native liver tissue to ensure an ethical and cost-effective approach [49]. Parameters such as thermal conductivity, electrical conductivity and density vary depending on tissue composition and differ between tumors and healthy liver parenchyma. These variations are further affected by cirrhosis, hepatic steatosis and prior treatments like systemic therapies or transarterial chemoembolization (TACE) [19]. Tissue properties of hepatic tumors and native liver parenchyma are well-documented and can directly be applied as parameters in the simulation software [39].

Both the *ex vivo* experimental setup as well as the numerical simulation represent simplified models of vascular cooling under controlled conditions and are not intended to fully reproduce physiological *in vivo* perfusion. The primary objective of this study was to assess the accuracy of the numerical simulation software, focusing on its ability to account for vascular cooling effects caused by a large vessel, rather than on reproducing the full complexity of hepatic vascular anatomy. To achieve a highly standardized yet experimentally demanding setup with a specific focus on localized cooling effects, a single saline-perfused glass tube was used to represent a large vessel. Previous research has demonstrated that glass tubes exhibit thermal properties comparable to those of hepatic vessels [50]. Within this controlled setting, the software successfully predicted cooling effects of large vessels. However, *in vivo* studies are required to investigate diffuse cooling, also known as 'perfusion-mediated tissue cooling', which arises from capillary liver perfusion [9]. This phenomenon limits the size of the ablation zone but does not alter its shape [31].

The use of a single vessel enabled reproducible positioning and systematic variation of vessel-antenna spacing, which is the primary factor affecting temperature distribution and vascular cooling effects [51,52]. We focused on systematically varying the vessel position rather than exploring hemodynamic parameters in detail, as these have been thoroughly investigated and were therefore not reexamined in the present study. While our setup inherently limited assessment of different vessel diameters and flow conditions – preventing a full sensitivity analysis – these parameters exert only limited influence beyond certain thresholds according to existing *ex vivo* and *in vivo* studies [29–32,53]. Accordingly, a saline flow rate of 100 ml/min and an outer vessel diameter of 5 mm were selected to ensure stable and reproducible cooling conditions. Our experiments were performed at room temperature. Because the thermal gradient relative to body temperature is higher under these conditions, cooling effects may appear more pronounced. This can be explained by the smaller thermal gradient between the ablation zone and the vessel at 37 °C compared with room temperature. However, previous studies indicate that macroscopic results obtained at room temperature and body temperature are generally comparable [32].

The multibipolar model employed in this study builds on a previously developed and validated numerical framework for mono- and bipolar hepatic RFA [17,21,22,38]. Electrical conductivity was modeled as a combined function of temperature, dehydration and coagulation via a predictor-corrector approach with Arrhenius damage modeling, rather than adopting purely temperature-based piecewise or exponential laws. While alternative piecewise-exponential formulations of temperature-dependent electrical conductivity have been proposed to improve accuracy especially at lower temperatures, comparative analyses have demonstrated only minor differences (<3.5%) in predicted ablation size between linear and exponential models [54–56]. In a high-temperature regime relevant for RFA, phase transitions and tissue dehydration – captured here through a predictor-corrector approach – predominantly govern electrical and thermal behavior [57]. Accordingly, the established formulation was retained.

The present study did not aim to introduce a novel temperature-dependent electrical conductivity formulation. Instead, our contribution lies in extending a validated modeling framework to multibipolar RFA in the presence of a vessel-mimicking glass tube and in its systematic validation against *ex vivo* experiments. Vessel and applicator interfaces were modeled using prescribed boundary conditions to ensure numerical stability and reproducibility. Model validation was restricted to a single, predefined vessel orientation relative to the applicators. The validity of the simulation for alternative configurations,

such as perpendicular vessel-applicator arrangements, was not assessed within the scope of this study. Validation was performed on a standardized two-dimensional cross-section of the ablation center, reflecting a highly controlled experimental setup with a specific focus on localized vascular cooling effects and minimizing registration uncertainty caused by tissue deformation and shrinkage. Although the simulation framework is capable of three-dimensional predictions, the present analysis was intentionally limited to a two-dimensional evaluation, single-plane evaluation. This prevented potential distortions of the ablation geometry associated with multiple sectioning of the soft liver tissue.

While the model reliably reproduced relative cooling patterns of large vessels under these standardized conditions, the results are limited to relative, localized cooling effects under controlled conditions. Further *in vivo* studies with three-dimensional validation are required to generalize predictions to whole ablation volumes.

Conclusion

This study advances numerical therapy planning for mbRFA, showing that the presented simulation provides accurate predictions of ablation outcomes and effectively models vascular cooling effects under standardized *ex vivo* conditions. The strong correlation between the predicted and the actual ablation zones underscores the simulation model's potential for enhancing mbRFA planning. However, further *in vivo* validation is essential to confirm these findings and optimize the integration of a numerical simulation for mbRFA into clinical routine.

Acknowledgement

Preliminary results from our study, titled '*Ex Vivo* Validation of a Numerical Simulation for Multipolar Radiofrequency Ablation', were presented by C. Rieder at the German Society for Computer- and Robot-Assisted Surgery conference (CURAC) and were featured in the conference proceedings [58].

Author contributions

CRediT: **Christina A. Neizert**: Conceptualization, Visualization, Writing – original draft, Writing – review & editing; **David Sinden**: Methodology, Software, Writing – review & editing; **Christian Rieder**: Software, Validation, Visualization, Writing – review & editing; **Tobias Preusser**: Software, Writing – review & editing; **Hanne Ballhausen**: Software, Writing – review & editing; **Ole Gemeinhardt**: Writing – review & editing; **Kai S. Lehmann**: Project administration, Resources, Supervision, Writing – review & editing; **Franz G. M. Poch**: Conceptualization, Formal analysis, Investigation, Methodology, Writing – original draft, Writing – review & editing.

Disclosure statement

No potential conflict of interest was reported by the author(s).

Funding

This research was funded by the *Deutsche Forschungsgemeinschaft* under grant number RI 1131/3-3.

ORCID

Christina A. Neizert http://orcid.org/0000-0003-2634-3602
David Sinden http://orcid.org/0000-0002-8514-8279

References

[1] Reig M, Forner A, Rimola J, et al. BCLC strategy for prognosis prediction and treatment recommendation: the 2022 update. J Hepatol. 2022;76(3):681–693. doi: 10.1016/j.jhep.2021.11.018.

[2] Izzo F, Granata V, Grassi R, et al. Radiofrequency ablation and microwave ablation in liver tumors: an update. Oncologist. 2019;24(10):e990–e1005. doi: 10.1634/theoncologist.2018-0337.
[3] Minami Y, Kudo M. Radiofrequency ablation of liver metastases from colorectal cancer: a literature review. Gut Liver. 2013;7(1):1–6. doi: 10.5009/gnl.2013.7.1.1.
[4] van der Lei S, Puijk RS, Dijkstra M, et al. Thermal ablation versus surgical resection of small-size colorectal liver metastases (COLLISION): an international, randomised, controlled, phase 3 non-inferiority trial. Lancet Oncol. 2025;26(2):187–199. doi: 10.1016/S1470-2045(24)00660-0.
[5] Vogl TJ, Martin SS, Gruber-Rouh T, et al. Comparison of microwave and radiofrequency ablation for the treatment of small- and medium-sized hepatocellular carcinomas in a prospective randomized trial. Rofo. 2024;196(5):482–490. doi: 10.1055/a-2203-2733.
[6] Gavriilidis P, Roberts KJ, de'Angelis N, et al. Recurrence and survival following microwave, radiofrequency ablation, and hepatic resection of colorectal liver metastases: a systematic review and network meta-analysis. Hepatobiliary Pancreat Dis Int. 2021;20(4):307–314. doi: 10.1016/j.hbpd.2021.05.004.
[7] Chai Y, Li K, Zhang C, et al. The short-term efficacy of no-touch radiofrequency ablation in treating cirrhosis-based small hepatocellular carcinoma. BMC Cancer. 2019;19(1):497. doi: 10.1186/s12885-019-5707-0.
[8] Mulier S, Ni Y, Jamart J, et al. Local recurrence after hepatic radiofrequency coagulation: multivariate meta-analysis and review of contributing factors. Ann Surg. 2005;242(2):158–171. doi: 10.1097/01.sla.0000171032.99149.fe.
[9] Goldberg SN, Hahn PF, Tanabe KK, et al. Percutaneous radiofrequency tissue ablation: does perfusion-mediated tissue cooling limit coagulation necrosis? J Vasc Interv Radiol. 1998;9(1 Pt 1):101–111. doi: 10.1016/s1051-0443(98)70491-9.
[10] Frericks BB, Ritz JP, Roggan A, et al. Multipolar radiofrequency ablation of hepatic tumors: initial experience. Radiology. 2005;237(3):1056–1062. doi: 10.1148/radiol.2373041104.
[11] Seror O, N'Kontchou G, Nault J-C, et al. Hepatocellular carcinoma within milan criteria: no-touch multibipolar radiofrequency ablation for treatment-long-term results. Radiology. 2016;280(2):611–621. doi: 10.1148/radiol.2016150743.
[12] Yap S, Cheong JKK, Ooi EH, et al. A numerical study on the no-touch bipolar radiofrequency ablation. Conf Proc IEEE Eng Med Biol Soc. 2019;2019:2887–2890.
[13] Ahmed M, Solbiati L, Brace CL, et al. Image-guided tumor ablation: standardization of terminology and reporting criteria—a 10-year update. Radiology. 2014;273(1):241–260. doi: 10.1148/radiol.14132958.
[14] Sato M, Tateishi R, Zohar Y, et al. Retrospective evaluation of a novel ultrasound-based imaging analysis software for predicting radiofrequency ablation areas. PLoS One. 2025;20(1):e0317469. doi: 10.1371/journal.pone.0317469.
[15] Schumann C, Rieder C, Bieberstein J, et al. State of the art in computer-assisted planning, intervention, and assessment of liver-tumor ablation. Crit Rev Biomed Eng. 2010;38(1):31–52. doi: 10.1615/critrevbiomedeng.v38.i1.40.
[16] Chen R, Zhang J, Kong D, et al. Fast calculation of 3D radiofrequency ablation zone based on a closed-form solution of heat conduction equation fitted by ex vivo measurements. Phys Med Biol. 2021;66(5):055022. doi: 10.1088/1361-6560/abe052.
[17] Rieder C, Kröger T, Schumann C, et al. GPU-based real-time approximation of the ablation zone for radiofrequency ablation. IEEE Trans Vis Comput Graph. 2011;17(12):1812–1821. doi: 10.1109/TVCG.2011.207.
[18] Mariappan P, Weir P, Flanagan R, et al. GPU-based RFA simulation for minimally invasive cancer treatment of liver tumours. Int J Comput Assist Radiol Surg. 2017;12(1):59–68. doi: 10.1007/s11548-016-1469-1.
[19] van Erp GCM, Hendriks P, Broersen A, et al. Computational modeling of thermal ablation zones in the liver: a systematic review. Cancers (Basel). 2023;15(23):5684. doi: 10.3390/cancers15235684.
[20] Hoffer EK, Drinane MC, Bhatnagar V, et al. Radiofrequency ablation of hepatocellular carcinoma guided by real-time physics-based ablation simulation: a prospective study. Int J Hyperthermia. 2024;41(1):2331704. doi: 10.1080/02656736.2024.2331704.
[21] Kroeger T, Paetz T, Altrogge I, et al. Fast estimation of the vascular cooling in RFA based on numerical simulation. Open Biomed Eng J. 2010;4:16–26.
[22] Kroeger T, Altrogge I, Preusser T, et al. Numerical simulation of radio frequency ablation with state dependent material parameters in three space dimensions. Med Image Comput Comput Assist Interv. 2006;9(Pt 2):380–388.
[23] Audigier C, Mohaiu AT, Alzaga A, et al. A comparative study on computational models of multi-electrode radiofrequency ablation of large liver tumors. Int J Comput Assist Radiol Surg. 2022;17(8):1489–1496. doi: 10.1007/s11548-022-02689-x.
[24] Rieder C, Poch F, Tiesler H, et al. Software Tool for the Analysis of the Coagulation Zone from Multipolar Radiofrequency Ablation. Deutsche Gesellschaft für Computer- und Roboterassistierte Chirurgie (CURAC); Vol. 1; 2012. p. 193–196.
[25] Vaidya N, Baragona M, Lavezzo V, et al. Simulation study of the cooling effect of blood vessels and blood coagulation in hepatic radio-frequency ablation. Int J Hyperthermia. 2021;38(1):95–104. doi: 10.1080/02656736.2020.1866217.
[26] Neizert CA, Do HNC, Zibell M, et al. Three-dimensional assessment of vascular cooling effects on hepatic microwave ablation in a standardized ex vivo model. Sci Rep. 2022;12(1):17061. doi: 10.1038/s41598-022-21437-4.
[27] Poch FGM, Neizert CA, Gemeinhardt O, et al. Intermittent Pringle maneuver may be beneficial for radiofrequency ablations in situations with tumor-vessel proximity. Innov Surg Sci. 2018;3(4):245–251. doi: 10.1515/iss-2018-0008.

[28] Poch FGM, Rieder C, Ballhausen H, et al. The vascular cooling effect in hepatic multipolar radiofrequency ablation leads to incomplete ablation ex vivo. Int J Hyperthermia. 2016;32(7):749–756. doi: 10.1080/02656736.2016.1196395.
[29] Poch FGM, Eminger KJ, Neizert CA, et al. Cooling effects occur in hepatic microwave ablation at low vascular flow rates and in close proximity to liver vessels – ex vivo. Surg Innov. 2022;29(6):705–715. doi: 10.1177/15533506221074619.
[30] Poch FG, Geyer B, Neizert CA, et al. Periportal fields cause stronger cooling effects than veins in hepatic microwave ablation: an in vivo porcine study. Acta Radiol. 2021;62(3):322–328. doi: 10.1177/0284185120928929.
[31] Lehmann KS, Ritz JP, Valdeig S, et al. Ex situ quantification of the cooling effect of liver vessels on radiofrequency ablation. Langenbecks Arch Surg. 2009;394(3):475–481. doi: 10.1007/s00423-009-0480-1.
[32] Lehmann KS, Poch FGM, Rieder C, et al. Minimal vascular flows cause strong heat sink effects in hepatic radiofrequency ablation ex vivo. J Hepatobiliary Pancreat Sci. 2016;23(8):508–516. doi: 10.1002/jhbp.370.
[33] Poch FGM, Rieder C, Ballhausen H, et al. Finding optimal ablation parameters for multipolar radiofrequency ablation. Surg Innov. 2017;24(3):205–213. doi: 10.1177/1553350617692492.
[34] Ringe KI, Lutat C, Rieder C, et al. Experimental evaluation of the heat sink effect in hepatic microwave ablation. PLoS One. 2015;10(7):e0134301. doi: 10.1371/journal.pone.0134301.
[35] Mulier S, Ni Y, Frich L, et al. Experimental and clinical radiofrequency ablation: proposal for standardized description of coagulation size and geometry. Ann Surg Oncol. 2007;14(4):1381–1396. doi: 10.1245/s10434-006-9033-9.
[36] Gemeinhardt O, Poch FGM, Hiebl B, et al. Comparison of bipolar radiofrequency ablation zones in an in vivo porcine model: correlation of histology and gross pathological findings. Clin Hemorheol Microcirc. 2016;64(3):491–499. doi: 10.3233/CH-168123.
[37] Rohlfing T, Maurer CR.Jr. Shape-based averaging. IEEE Trans Image Process. 2007;16(1):153–161. doi: 10.1109/tip.2006.884936.
[38] Altrogge I, Preusser T, Kroger T, et al. Sensitivity analysis for the optimization of radiofrequency ablation in the presence of material parameter uncertainty. Int J UncertaintyQuantification. 2012;2(3):295–321. doi: 10.1615/Int.J.UncertaintyQuantification.2012004135.
[39] Zurbuchen U, Poch F, Gemeinhardt O, et al. Determination of the electrical conductivity of human liver metastases: impact on therapy planning in the radiofrequency ablation of liver tumors. Acta Radiol. 2016;58(2):164–169. doi: 10.1177/0284185116639765.
[40] Pennes HH. Analysis of tissue and arterial blood temperatures in the resting human forearm. J Appl Physiol. 1948;1(2):93–122. doi: 10.1152/jappl.1948.1.2.93.
[41] Dice LR. Measures of the amount of ecologic association between species. Ecology. 1945;26(3):297–302. doi: 10.2307/1932409.
[42] Jaccard P. The distribution of the flora of the alpine zone. New Phytol. 1912;11(2):37–50. doi: 10.1111/j.1469-8137.1912.tb05611.x.
[43] Voglreiter P, Mariappan P, Pollari M, et al. RFA guardian: comprehensive simulation of radiofrequency ablation treatment of liver tumors. Sci Rep. 2018;8(1):787. doi: 10.1038/s41598-017-18899-2.
[44] Moche M, Busse H, Futterer JJ, et al. Clinical evaluation of in silico planning and real-time simulation of hepatic radiofrequency ablation (ClinicIMPPACT Trial). Eur Radiol. 2020;30(2):934–942. doi: 10.1007/s00330-019-06411-5.
[45] Laimer G, Schullian P, Jaschke N, et al. Minimal ablative margin (MAM) assessment with image fusion: an independent predictor for local tumor progression in hepatocellular carcinoma after stereotactic radiofrequency ablation. Eur Radiol. 2020;30(5):2463–2472. doi: 10.1007/s00330-019-06609-7.
[46] Wong SL, Mangu PB, Choti MA, et al. American Society of Clinical Oncology 2009 clinical evidence review on radiofrequency ablation of hepatic metastases from colorectal cancer. J Clin Oncol. 2010;28(3):493–508. doi: 10.1200/JCO.2009.23.4450.
[47] Hoffer EK, Borsic A, Patel SD. Validation of software for patient-specific real-time simulation of hepatic radiofrequency ablation. Acad Radiol. 2022;29(10):e219–e27. doi: 10.1016/j.acra.2021.12.018.
[48] Ruiter SJS, Heerink WJ, de Jong KP. Liver microwave ablation: a systematic review of various FDA-approved systems. Eur Radiol. 2019;29(8):4026–4035. doi: 10.1007/s00330-018-5842-z.
[49] Mishima K, Itano O, Matsuda S, et al. Development of human hepatocellular carcinoma in X-linked severe combined immunodeficient pigs: an orthotopic xenograft model. PLoS One. 2021;16(3):e0248352. doi: 10.1371/journal.pone.0248352.
[50] Welp C, Siebers S, Ermert H, et al. Investigation of the influence of blood flow rate on large vessel cooling in hepatic radiofrequency ablation. Biomed Tech (Berl). 2006;51(5-6):337–346. doi: 10.1515/BMT.2006.067.
[51] Wang J, Wu S, Wu Z, et al. Influences of blood flow parameters on temperature distribution during liver tumor microwave ablation. Front Biosci (Landmark Ed). 2021;26(9):504–516. doi: 10.52586/4963.
[52] Poch FGM, Neizert CA, Geyer B, et al. Influence of interapplicator distance on multibipolar radiofrequency ablation during physiological and interrupted liver perfusion in an in vivo porcine model. Sci Rep. 2020;10(1):16210. doi: 10.1038/s41598-020-71512-x.
[53] Chiang J, Hynes K, Brace CL. Flow-dependent vascular heat transfer during microwave thermal ablation. Annu Int Conf IEEE Eng Med Biol Soc. 2012;2012:5582–5585. doi: 10.1109/EMBC.2012.6347259.
[54] Trujillo M, Berjano E. Review of the mathematical functions used to model the temperature dependence of electrical and thermal conductivities of biological tissue in radiofrequency ablation. Int J Hypertherm. 2013;29(6):590–597. doi: 10.3109/02656736.2013.807438.
[55] Castro-Lopez DL, Trujillo M, Berjano E, et al. Two-compartment mathematical modeling in RF tumor ablation: new insight when irreversible changes in electrical conductivity are considered. Math Biosci Eng. 2020;17(6):7980–7993.

[56] Possebon R, Jiang Y, Mulier S, et al. A piecewise function of resistivity of liver: determining parameters with finite element analysis of radiofrequency ablation. Med Biol Eng Comput. 2018;56(3):385–394. doi: 10.1007/s11517-017-1699-6.
[57] Silva NP, Bottiglieri A, Conceição RC, et al. Characterisation of ex vivo liver thermal properties for electromagnetic-based hyperthermic therapies. Sensors (Basel). 2020;20(10):3004. doi: 10.3390/s20103004.
[58] Rieder C, Ballhausen H, Poch FGM, et al. Ex vivo validation of a numerical simulation for multipolar radiofrequency ablation. Deutsche Gesellschaft für Computer- und Roboterassistierte Chirurgie (CURAC). Bremen, Germany; 2015. p. 55–60.

Appendix A

The material properties are computed using interpolation from piece-wise polynomial segments over small temperature intervals. Note that no hysteresis effects are included, which given a single cycle of heating was performed, is a justifiable assumption.

The electrical conductivity is linearly dependent on temperature, coagulation and dehydration. The dependence on each factor is applied separately, so that the temperature-dependent electrical conductivity is scale by the water content ratio, and then the coagulation ratio. The water content and coagulation are both temperature dependent, with coagulation being directly determined by the temperature-dependent damage integral:

$$\sigma(\mathrm{T},\gamma,\Omega)=\sigma_T(T)\cdot\sigma_\gamma(\gamma)\cdot\sigma_\Omega(\Omega) \tag{8}$$

For $\sigma_T=\sigma_0+(T-T_0)\sigma_1^T$, where σ_0=0.306 [S/m] is the base value at room temperature, T_0, and σ_1^T = 0.17, which characterizes the linear increase in the electrical conductivity with respect to temperature. The dehydration factor is given by

$$\sigma_\gamma=\sigma_0+(\mathrm{T}-\mathrm{T}_0)\sigma_1 \tag{9}$$

So that when T=100, $\sigma_\gamma=0$. Similarly, for coagulation

$$\sigma_\cdot=\sigma_0+(T-T_0)\sigma_1^\Omega \tag{10}$$

where σ_0 is the baseline value, and σ_1^Ω is such that at T=100 then σ_Ω=0.45. The thermal conductivity is modeled as quadratic function of temperature up to 90 °C, and then as a linear function of temperature.

$$k=\begin{cases}k_2T^2+k_1T+k_0, & T<90\\ \tilde{k}_1T+\tilde{k}_0, & T\geq 90\end{cases} \tag{11}$$

k_0	0.594727	W/(m·K)
k_1	−0.004702	W/(m·K^2)
k_2	7.25253E-7	W/(m·K^3)
$\tilde{k}_0$	0.706636	W/(m·K)
$\tilde{k}_1$	0.0005818	W/(m·K^2)

The specific heat capacity properties and density are derived from Equation (6). The specific heat follows the same quadratic-linear relationship as the thermal conductivity.

$$c=\begin{cases}c_2T^2+c_1T+c_0 & T<90\\ \tilde{c}_1T+\tilde{c}_0 & T\geq 90\end{cases} \tag{12}$$

c_0	0.594727	J/(kg·K)
c_1	−0.004702	J/(kg·K^2)
c_2	7.25253E-7	J/(kg·K^3)
$\tilde{c}_0$	0.706636	J/(kg·K)
$\tilde{c}_1$	0.0005818	J/(kg·K^2)

The Arrhenius rate parameters are derived from Equation (7), where the universal gas constant is given by R_g= 8.314 [J mol/K], the activation energy is E_a= 257,700 [J/mol] and the frequency factor A_0= 7.39×10^{39} [1/s].